

Dominant two-dimensional electron-phonon interactions in the bulk Dirac semimetal Na_3Bi

Dhruv C. Desai,^{†,§} Jinsoo Park,^{†,§} Jin-Jian Zhou,[‡] and Marco Bernardi^{*,†,¶}

[†]*Department of Applied Physics and Materials Science, California Institute of Technology, Pasadena, California 91125, USA.*

[‡]*School of Physics, Beijing Institute of Technology, Beijing 100081, China.*

[¶]*Department of Physics, California Institute of Technology, Pasadena, California 91125, USA*

[§]*D.D. and J.P. contributed equally to this work*

E-mail: bmarco@caltech.edu

Abstract

Bulk Dirac semimetals (DSMs) exhibit unconventional transport properties and phase transitions due to their peculiar low-energy band structure. Yet the electronic interactions governing nonequilibrium phenomena in DSMs are not fully understood. Here we show that electron-phonon (e -ph) interactions in a prototypical bulk DSM, Na_3Bi , are predominantly two-dimensional (2D). Our first-principles calculations discover a 2D optical phonon with strong e -ph interactions associated with in-plane vibrations of Na atoms. We show that this 2D mode governs e -ph scattering and charge transport in Na_3Bi , and induces a dynamical phase transition to a Weyl semimetal. Our work advances quantitative analysis of electron interactions in topological semimetals and reveals dominant low-dimensional interactions in bulk quantum materials.

Topological semimetals are characterized by electronic band crossings near the Fermi energy, which result in linear band dispersions and topologically nontrivial band structures.¹ There is a vast literature on their unusual properties, including high mobility and magnetoresistance,^{2–8} anomalous transport regimes,^{8–10} surface Fermi arcs,^{11–14} and topological phase transitions.^{15,16} The discovery of graphene – a two-dimensional Dirac semimetal (DSM) – has enabled studies of new physics in a carbon atom sheet.¹⁷ In contrast with graphene, three-dimensional (bulk) DSMs are materials with rich structural and chemical complexity. They present a wide range of possible crystal structures and arrangements of Dirac cones, whose degeneracy is protected by crystal symmetry,¹ which makes bulk DSMs interesting for device applications.^{18,19}

Although many properties of DSMs can be explained using model low-energy Hamiltonians, the interactions between electrons and other degrees of freedom – such as phonons, photons, and spin – are not simple to quantify and give rise to rich physics in DSMs. Examples include phonon nonlinearities, unconventional nonequilibrium dynamics, and topological phase transitions,^{20–24} among others. Electron-phonon (*e-ph*) interactions play a central role in this physics, but their understanding in bulk DSMs – and more generally in topological semimetals – is rather limited and relies mainly on phenomenological models.^{25,26} First-principles calculations of *e-ph* interactions, which have now been applied to many classes of materials,^{27–38} have been hindered in bulk DSMs by their complex atomic and electronic structures.

Sodium bismuthate (Na_3Bi) is a prototypical bulk DSM^{11,39} whose Dirac cones have been observed by scanning tunneling spectroscopy,^{16,40–42} angle-resolved photoemission (ARPES),^{12,39} and transport measurements.⁸ In Na_3Bi , first-principles calculations have examined impurity-limited transport,⁴³ nonequilibrium dynamics,⁴⁴ and spin-orbit coupling.⁴⁵ However, a quantitative analysis of *e-ph* interactions is still missing. The interplay between crystal symmetry and electron spin, orbital, and momentum degrees of freedom suggests that Na_3Bi and other

bulk DSMs may host unconventional e -ph interactions yet to be discovered. We explore this direction by carrying out a detailed first-principles study of e -ph interactions in Na₃Bi. We use density functional theory (DFT)^{46,47} to obtain the electronic structure, lattice vibrations, and their interactions; our calculations take into account spin-orbit coupling (SOC) and many-body corrections to the electronic band structure (with the GW method⁴⁸), and employ an improved treatment of acoustic phonons (see Methods).

Leveraging these accurate tools, we discover a dominant two-dimensional (2D) e -ph interaction in Na₃Bi associated with a 2D optical phonon with e -ph coupling strength far greater than that of any other mode. Our analysis shows that this 2D e -ph interaction governs the scattering and transport of Dirac electrons, and reveals its microscopic origin. Similar “killer” phonon modes with dominant e -ph coupling controlling charge transport have been found in organic crystals⁴⁹ but not in topological materials. We also find that the strongly-coupled 2D mode breaks inversion symmetry in Na₃Bi and induces a dynamical phase transition to a Weyl semimetal (WSM). This finding points to new opportunities for ultrafast control of topological materials.^{20–24,44}

The unit cell of Na₃Bi, shown in Figure 1a, belongs to the hexagonal $P6_3/mmc$ space group. Its crystal structure alternates a layer of Bi plus Na atoms, labeled Na(1), and a layer made up only by Na atoms, labeled Na(2). Inversion plus C_3 rotational symmetry result in a four-fold band degeneracy near the Fermi energy, with contributions from Na 3s and Bi 6p orbitals.^{11,42,50–52} The Dirac cone is made up by two electronic bands, one with Na 3s + Bi 6p_z and the other with Bi 6p_x + 6p_y orbital character (the latter is denoted below as Bi- p_{xy} band). To obtain an accurate band structure, we start from DFT and then apply a one-shot GW correction (see Methods), which increases the velocity of the Na 3s + Bi 6p_z band by a factor of 1.8 and reduces the velocity of the Bi p_{xy} -band relative to DFT (Figure 1b,c). The Fermi velocity computed with GW about 300 meV above the Dirac node is $7.0 \times 10^5 \text{ ms}^{-1}$, in excellent agreement with the experimental value of $8.1 \times 10^5 \text{ ms}^{-1}$.⁹ Our computed GW band structure agrees well with ARPES measurements by Liang et al.¹² (See Supplementary

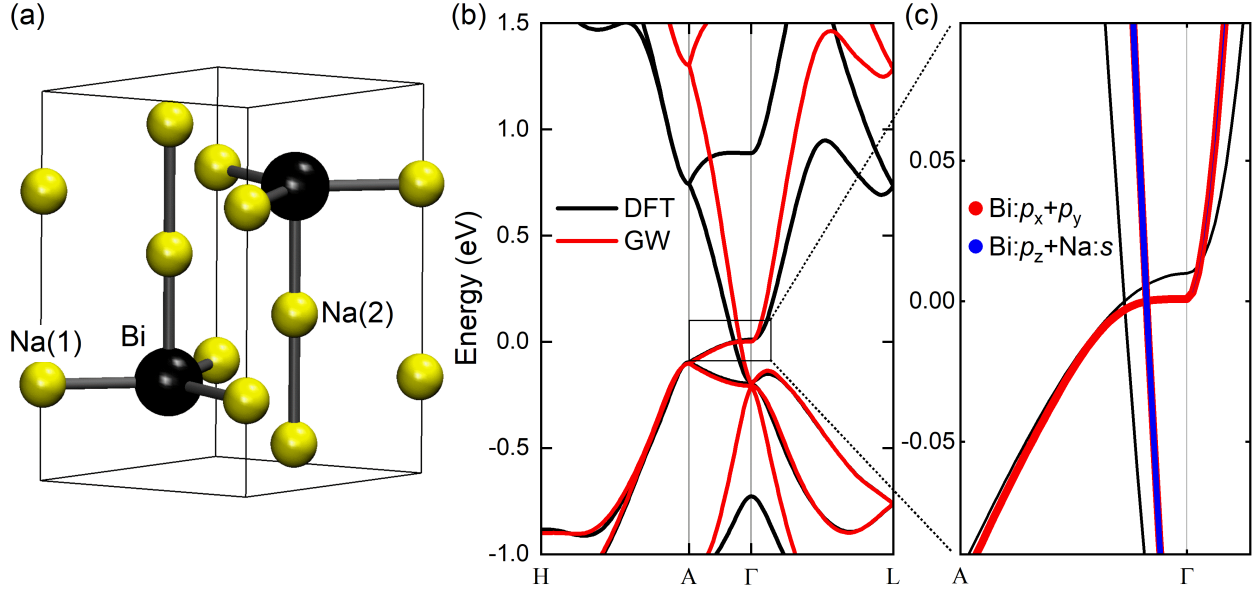


Figure 1: (a) Crystal structure of Na₃Bi with $P6_3/mmc$ space-group symmetry. The Bi (Na) atoms are shown with black (yellow) spheres. (b) Band structure of Na₃Bi comparing DFT (black) and GW (red) results. (c) Zoom-in of the band structure in (b) near the Dirac point, with states color-coded according to their orbital character.

information).

The computed phonon dispersion in Na₃Bi is shown in Figure 2a. The phonon frequencies are positive for all modes (color-coded curves in Figure 2a), indicating a dynamically stable $P6_3/mmc$ crystal structure with no soft modes or imaginary frequencies. Fine-tuning the acoustic sum rule is crucial to obtaining this well-behaved phonon dispersion. Our results employ an advanced acoustic sum rule which minimally affects the inter-atomic force constants from DFPT,⁵³ conversely, a widely-used – so-called “simple” – acoustic sum rule,⁵⁴ which modifies the inter-atomic force constants to enforce translational symmetry, leads to spurious soft phonons near the K-point of the Brillouin zone⁵⁵ (gray curves in Figure 2a).

Our settings, which combine a stable crystal structure, well-defined phonon dispersions, and electronic states with an accurate Fermi velocity allow us to carry out reliable first-principles calculations of e -ph interactions in Na₃Bi.³¹ We compute the e -ph matrix elements $g_{mn\nu}(\mathbf{k}, \mathbf{q})$, which encode the e -ph coupling between pairs of electronic states (initial state $|n\mathbf{k}\rangle$ and final state $|m\mathbf{k} + \mathbf{q}\rangle$, where n and m are band indices and \mathbf{k} the electron crystal

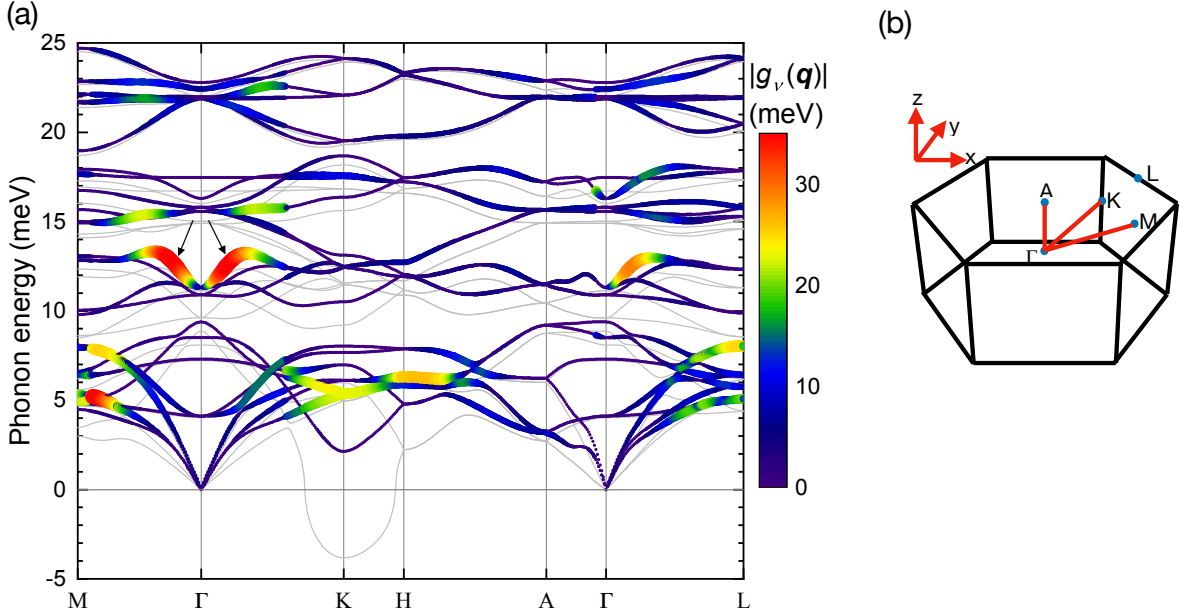


Figure 2: (a) Na_3Bi phonon dispersion overlaid with a color map of the e -ph coupling strength, $|g_\nu(\mathbf{q})|$, for wave-vector \mathbf{q} along high-symmetry lines. The marker size is proportional to $|g_\nu(\mathbf{q})|$ and the arrows indicate the strongly-coupled 2D phonon mode. The phonon dispersion obtained with the simple acoustic sum rule is shown for comparison using gray lines, with imaginary frequencies shown as negative values. (b) Brillouin zone of Na_3Bi , shown to aid the interpretation of panel (a). The $\Gamma - M$ and $\Gamma - K$ directions are in the xy -plane, and $\Gamma - A$ corresponds to the z -direction.

momentum) due to a phonon with mode index ν and wave-vector \mathbf{q} . These calculations are carried out with the PERTURBO code⁵⁶ as described in Methods.

Figure 2 shows the phonon dispersion in Na_3Bi overlaid with a color map of the e -ph coupling strength, defined as $|g_\nu(\mathbf{q})| \equiv (\sum_{mn} |g_{mn\nu}(\mathbf{k} = 0, \mathbf{q})|^2 / N_b)^{1/2}$ (here we sum over $N_b = 2$ lowest conduction bands).⁵⁶ We find that the e -ph interactions are overall relatively weak in Na_3Bi , with an average value $|g_\nu(\mathbf{q})| \approx 5$ meV. Yet one particular phonon mode, with ~ 12 meV energy and wave-vector \mathbf{q} in the $\Gamma - M$ and $\Gamma - K$ directions (which correspond to the crystal xy -plane; see Figure 2b) exhibits a much stronger e -ph coupling than any other mode, with value $|g| \approx 35$ meV. This strongly-coupled 2D mode is a longitudinal optical (LO) phonon that is infrared-active and has E_{1u} character at the zone center.⁵⁷ Its associated atomic vibrations, shown in Figure 3a, have primary contributions from Na(2) atoms, which

oscillate with large amplitudes in the Na-only layers of Na₃Bi, and have negligible contributions from the Na(1) and Bi atoms in the neighboring layers. Because the wave-vector and atomic displacements of this strongly-coupled 2D mode are both in the xy -plane, the dominant e -ph interactions in Na₃Bi are inherently two-dimensional.

To understand the microscopic origin these strong 2D e -ph interactions, we analyze their perturbation potential, whose local lattice-periodic part can be written as^{47,56}

$$\Delta V_{\nu\mathbf{q}}(\mathbf{r}) \equiv \sum_{\kappa} \frac{1}{\sqrt{M_{\kappa}}} \mathbf{e}_{\nu\mathbf{q}}^{(\kappa)} \cdot \partial_{\kappa,\mathbf{q}} V(\mathbf{r}) , \quad (1)$$

where M_{κ} is the mass and $\mathbf{e}_{\nu\mathbf{q}}^{(\kappa)}$ the displacement eigenvector of atom κ due to phonon mode (ν, \mathbf{q}) , and $\partial_{\kappa,\mathbf{q}} V(\mathbf{r})$ is the derivative of the local Kohn-Sham potential with respect to the position of atom κ .⁵⁶ We focus on the effect of the dominant Na(2) atomic vibrations on the Bi- p_{xy} Dirac-cone electronic states near Γ . Figure 3 shows the e -ph perturbation potential $\Delta V_{\nu\mathbf{q}}(\mathbf{r})$ generated by Na(2) atomic vibrations and plotted in the xy -plane containing Bi atoms. For the dominant 2D LO mode (Figure 3a), which has wave-vector \mathbf{q} in the xy -plane, the Na(2) atoms move out-of-phase within each layer, causing large perturbations at the Bi atoms. As a result electronic states in the Bi p_{xy} -band couple strongly with this phonon mode. Increasing $|\mathbf{q}|$ in the xy -plane leads to an even greater perturbation at the Bi site and thus stronger e -ph coupling. In contrast, for a 2D transverse optical mode propagating in the z -direction the Na(2) atoms move uniformly in-phase in the xy -plane (Figure 3b). In this case, $\Delta V_{\nu\mathbf{q}}(\mathbf{r})$ has a symmetric pattern with nodes at Bi atoms, which suppresses e -ph coupling for the Bi- p_{xy} band. Accordingly, we find a very weak e -ph coupling for such transverse optical modes, as shown by the dark blue color in the Γ -A direction in Figure 2a.

We analyze two important consequences of the strong 2D e -ph coupling in Na₃Bi. First, we find that charge transport is governed by scattering of Dirac electrons with the strongly-coupled 2D mode, which contributes nearly half of the total e -ph scattering rate (Figure 4a) and resistivity (see below). Other individual phonon modes contribute significantly less, up to 15% of the e -ph scattering rate for the mode with the second strongest coupling.

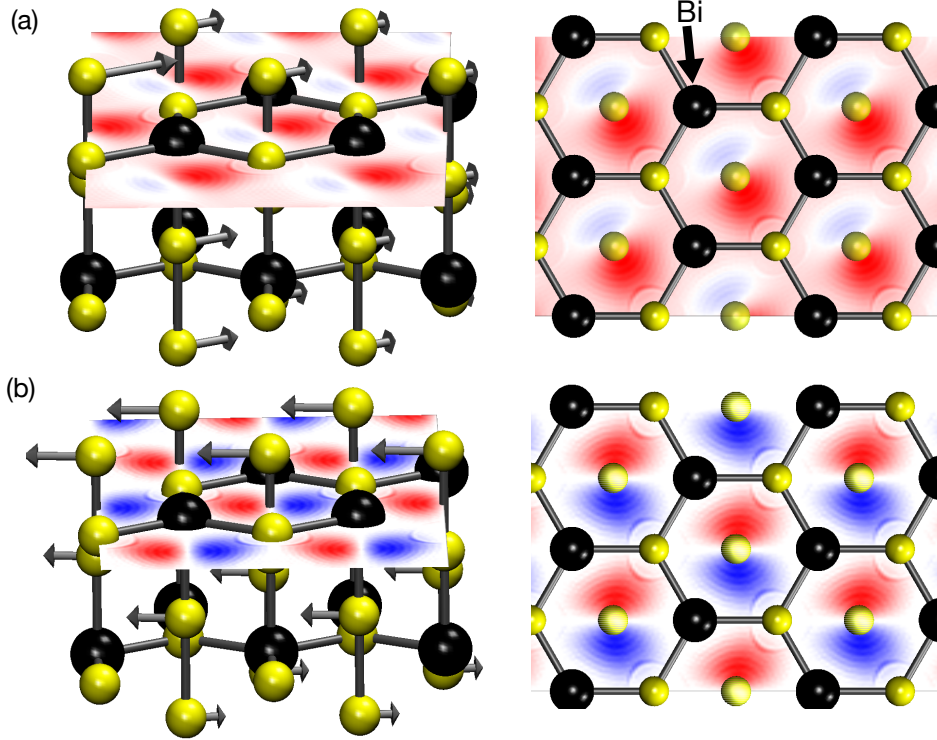


Figure 3: Side view (left) and top view (right) of atomic motions and e -ph perturbation potentials $\Delta V_{\nu\mathbf{q}}(\mathbf{r})$ for two phonon modes: (a) Strongly-coupled 2D longitudinal optical phonon with wave-vector $\mathbf{q}=(1/6,0,0)$ in the xy -plane, associated with a large perturbation at the Bi site leading to strong e -ph interactions; (b) transverse optical mode with $\mathbf{q} = (0,0,1/8)$ along the z -axis, resulting in a negligible e -ph coupling due to the weak perturbation at the Bi site. In both cases, we compute $\Delta V_{\nu\mathbf{q}}(\mathbf{r})$ from Na(2) atomic vibrations and plot it in the xy -plane containing Bi and Na(1) atoms. Red and blue colors correspond to positive and negative values of $\Delta V_{\nu\mathbf{q}}(\mathbf{r})$, respectively.

Therefore, this strongly-coupled 2D LO mode is analogous to the “killer” phonons controlling charge transport recently discovered in organic crystals.⁴⁹

Because of the strong 2D e -ph coupling, Dirac-cone electronic states with in-plane momentum \mathbf{k} , which couple to each other via phonons with in-plane momenta, exhibit large e -ph scattering rates (Figure 4b). In contrast, electrons with momentum \mathbf{k} in the z -direction scatter mostly via phonons with out-of-plane \mathbf{q} , and are associated with smaller scattering rates. This anisotropic scattering due to 2D e -ph coupling is evident in the entire temperature range we analyzed (77–300 K). We have verified that the e -ph matrix elements $g(\mathbf{k}, \mathbf{q})$

possess a similar anisotropy, such that the e -ph coupling strength $|g(\mathbf{k}, \mathbf{q})|$ is much greater for in-plane than for out-of-plane electron momenta.

We compute the phonon-limited mobility and resistivity using these first-principles e -ph scattering rates in the Boltzmann transport equation⁵⁶ (see Methods). Our results show that the in-plane mobility for temperatures between 150–400 K is very large (Figure 4c) – up to $\sim 30,000$ cm²/Vs at room temperature and high electron concentration, mainly as a result of the high Fermi velocity of the Bi p_{xy} -band and the overall weak e -ph coupling. This mobility limit, which applies to an ideally pure crystal of Na₃Bi where charge transport is impeded only by phonons, is exceptionally high and has the same order of magnitude as the mobility in graphene.¹⁷ To our knowledge, such large electron mobilities have not yet been measured in Na₃Bi near room temperature; one possible reason is that Na₃Bi samples typically contain large concentrations of defects, particularly Na vacancies, which may make the intrinsic phonon-limited mobility difficult to observe.^{40,41} Improvements in growth techniques may bring the experimental mobility of Na₃Bi closer to our predicted theoretical limit. Note that in Cd₃As₂, a widely studied DSM, mobility values as high as $\sim 40,000$ cm²/Vs at 130 K have been reported,⁵⁸ which are comparable to the $\sim 100,000$ cm²/Vs we predict in Na₃Bi for the same temperature and carrier concentration.

To complete our discussion on transport, Figure 4d shows the computed in-plane resistivity as a function of temperature for Fermi energies between 100–300 meV. In this regime, the transport behavior is metallic, and the resistivity increases with temperature following a power law. Comparison with experiments is important despite the variability in Na₃Bi sample quality noted above. We compare our calculations with the measurements by Xiong *et al.*,⁹ which achieve the lowest resistivity among available experimental data^{9,40} indicating higher sample quality. Our computed resistivity is lower than their measured values⁹ by about an order of magnitude at 50 K and a factor of 3–5 at 250 K. The lower discrepancy at higher temperature indicates an improved agreement between theory and experiment in the intrinsic, phonon-limited transport regime studied in this work.

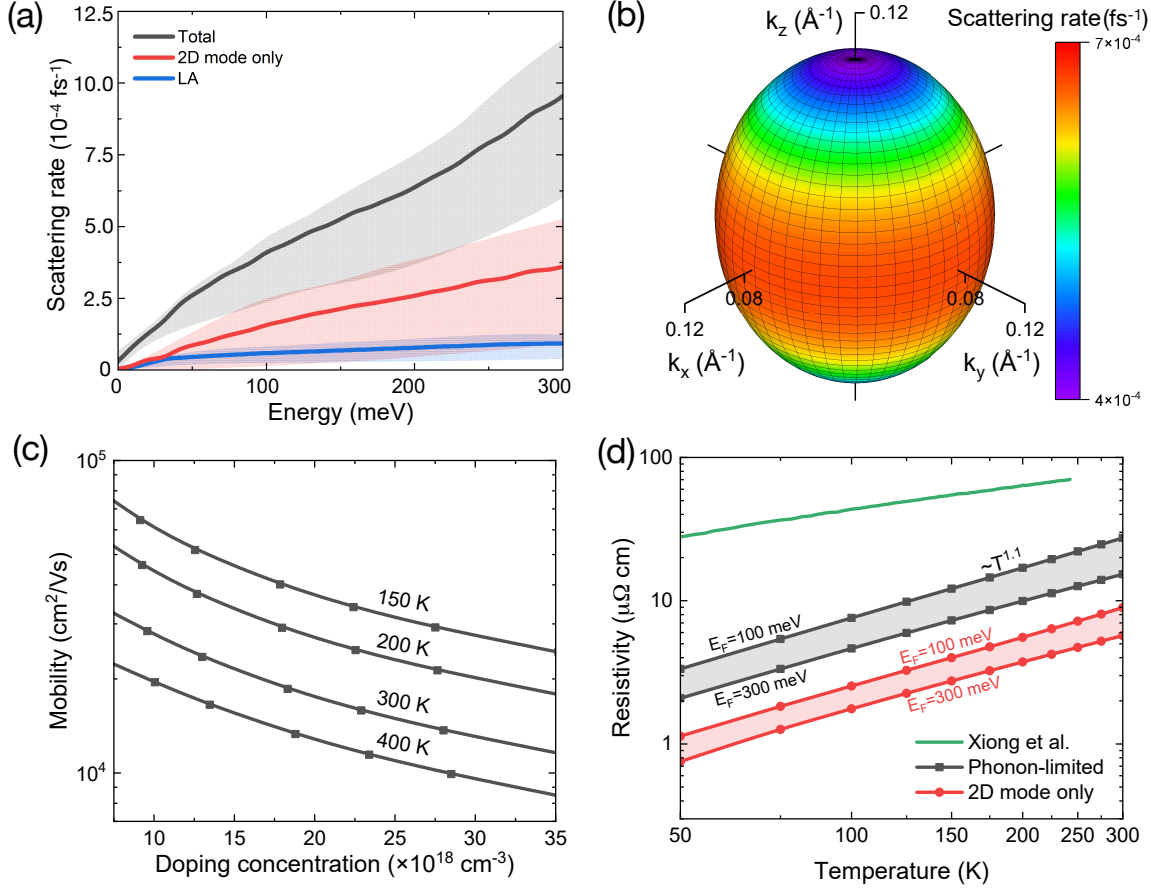


Figure 4: Calculations of transport and e -ph scattering in Na₃Bi. (a) E -ph scattering rates as a function of carrier energy at 300 K and $E_F = 200 \text{ meV}$. We show the total scattering rate (black) and the contributions from the strongly-coupled 2D mode (red) and the longitudinal acoustic (LA) mode with second strongest coupling (blue). For each curve, we plot the average scattering rate with a solid line, and show the standard deviation as a shaded region. (b) Fermi surface at $E_F = 200 \text{ meV}$ color-coded according to the total e -ph scattering rates. (c) Electron mobility as a function of carrier concentration for temperatures between 150–400 K. (d) Temperature dependent resistivity for Fermi energies between 100–300 meV above the Dirac point, shown together with the strongly-coupled 2D-mode contribution. Experimental results by Xiong et al.⁹ are shown for comparison.

It is interesting to compare these findings with graphene, a 2D DSM. In both Na₃Bi and graphene, a 2D optical phonon has the strongest e -ph coupling.^{59,60} However, heavier atoms and weaker bonding in Na₃Bi result in softer phonons – the energy of the strongly-coupled 2D phonon in Na₃Bi is only $\sim 12 \text{ meV}$, and thus much smaller than the $\sim 200 \text{ meV}$ energy of strongly-coupled 2D optical phonons in graphene.⁶⁰ At room temperature, where $k_B T \approx 26 \text{ meV}$, the strongly-coupled 2D phonons are thermally excited in Na₃Bi, while in

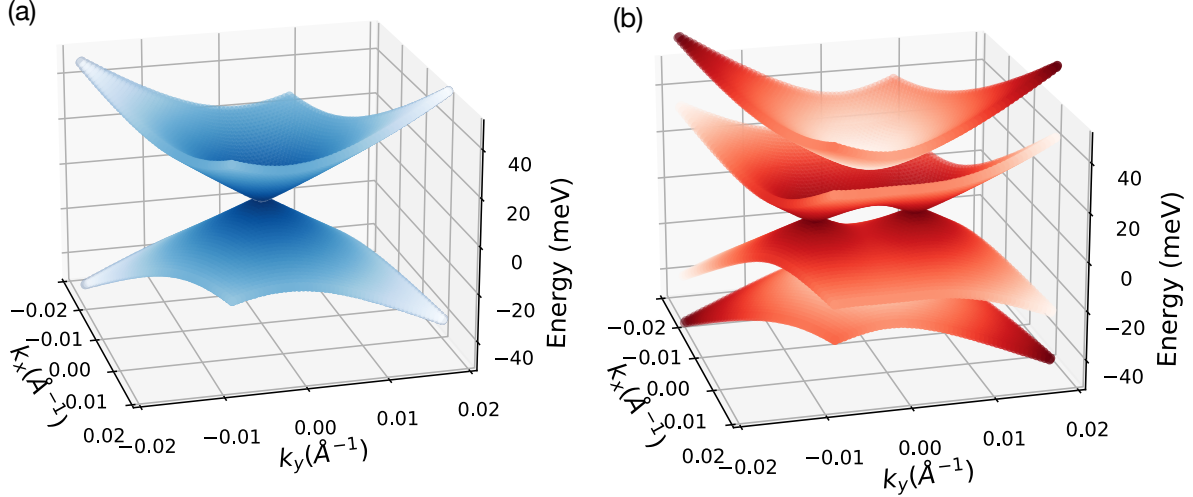


Figure 5: Electronic band structure computed with DFT for (a) pristine and (b) 2D-mode distorted Na_3Bi . The displacement in (b) is 3% of the in-plane lattice constant.

graphene only acoustic phonons are present. As a result, optical modes contribute less than 15% to the resistivity in graphene at 300 K,⁶¹ versus a dominant 50% resistivity contribution from the strongly-coupled 2D phonon in Na_3Bi (Figure 4d). Note that while graphene is a 2D material, Na_3Bi is a bulk crystal where a dominant 2D e -ph interaction is unexpected.

Finally, we find that the atomic vibrations from the strongly-coupled 2D mode dynamically induce a phase transition to a Weyl semimetal (WSM) in Na_3Bi . Due to its E_{1u} character,⁵⁷ this 2D mode dynamically breaks inversion symmetry and removes the four-fold degeneracy at the Dirac point, splitting each Dirac cone into a pair of Weyl cones. Figure 5 shows the DFT band structure in the k_x - k_y plane containing the Dirac node, comparing results for the pristine structure (Figure 5a) and for the lattice distorted from the strongly-coupled 2D mode (Figure 5b), which is computed with frozen-in atomic displacements along the 2D-mode eigenvector (see Methods). The atomic displacements split each Dirac node into a pair of Weyl nodes separated along k_y by about 0.01 \AA^{-1} ; the system remains metallic throughout this phase transition. Inversion symmetry breaking from the strongly-coupled E_{1u} mode is crucial to obtaining the WSM phase: phonon distortions that preserve inversion symmetry but break the threefold rotational symmetry – for example, E_{2g} modes, which

are however weakly coupled – are not robust against a gap opening, and instead cause a phase transition to a topological insulator.

These results imply that 2D phonons with strong e -ph coupling can provide a versatile knob for ultrafast control in Na_3Bi . In particular, because the strongly-coupled 2D LO mode is infrared active⁶² (but not Raman active), one could induce a topological phase transition in Na_3Bi by coherently driving this 2D mode using a THz pulse⁶³ or through carrier optical excitation followed by strong e -ph coupling.⁶³ Interestingly, Hübener et al.⁴⁴ have shown that a similar phase transition from a DSM to a WSM can be achieved in Na_3Bi with a different mechanism – strong light-matter coupling, which dresses the electronic states inducing Floquet-Weyl nodes. These predictions contribute to the thriving area of driven nonequilibrium dynamics in topological materials, where recent experiments on bulk DSMs²² and WSMs^{20,21} have demonstrated nonequilibrium topological phase transition using electric fields or optical pulses.

In conclusion, we have shown that the dominant e -ph interactions in a prototypical bulk DSM, Na_3Bi , are inherently two-dimensional and govern the scattering and transport of Dirac electrons. Our first-principles analysis reveals the microscopic origin of this strong 2D e -ph coupling; it also shows that the strongly-coupled 2D mode can induce a dynamical phase transition to a WSM, suggesting new routes for ultrafast control of Dirac electrons in bulk DSMs. These results seed the question of whether other bulk materials may host dominant low-dimensional e -ph interactions governing their physical properties. For example, MgB_2 , a superconductor with a relatively high critical temperature of ~ 40 K, has a crystal structure similar to Na_3Bi and has been hypothesized to host a 2D phonon with strong e -ph coupling.^{64,65} First-principles calculations such as those shown in this work can contribute to address these questions and advance future discoveries of electronic interactions and nonequilibrium dynamics in topological materials.

Methods

DFT, DFPT and GW calculations

We perform DFT calculations in a plane-wave basis set using the QUANTUM ESPRESSO⁵⁴ code. We employ the PBEsol⁶⁶ exchange-correlation functional and fully-relativistic norm-conserving pseudopotentials from Pseudo Dojo.⁶⁷ These calculations use a coarse $12 \times 12 \times 8$ \mathbf{k} -point grid, a kinetic energy cutoff of 90 Ry, and relaxed lattice constants ($a = 5.42$ Å and $c = 9.67$ Å) which are in excellent agreement with the experimental values ($a = 5.45$ Å and $c = 9.66$ Å).¹¹ The phonon dispersions and perturbation potentials are computed using coarse grids with $6 \times 6 \times 8$ \mathbf{q} -points using DFPT.⁴⁷ We employ the crystal acoustic sum rule from Ref.⁵³ to compute phonon dispersions. The GW correction to the electronic band structure is computed using the YAMBO code.⁶⁸ We employ 120 unoccupied bands and a 10 Ry energy cutoff for the dielectric screening combined with the Bruneval-Gonze terminator;⁶⁹ we have verified that increasing the number of unoccupied bands to 600 and the energy cutoff to 30 Ry has a negligible effect.

Electron-phonon matrix elements and perturbation potentials

We use the PERTURBO code⁵⁶ to obtain the e -ph coupling matrix elements on the coarse \mathbf{k} - and \mathbf{q} -point grids given above. The e -ph matrix elements $g_{m\nu}(\mathbf{k}, \mathbf{q})$ are defined as

$$g_{m\nu}(\mathbf{k}, \mathbf{q}) = \sqrt{\frac{\hbar}{2\omega_{\nu\mathbf{q}}}} \langle \psi_{m\mathbf{k}+\mathbf{q}} | \Delta V_{\nu\mathbf{q}} | \psi_{n\mathbf{k}} \rangle, \quad (2)$$

where $|\psi_{n\mathbf{k}}\rangle$ and $|\psi_{m\mathbf{k}+\mathbf{q}}\rangle$ are Bloch states with momenta \mathbf{k} and $\mathbf{k} + \mathbf{q}$, and $\Delta V_{\nu\mathbf{q}}$ is the lattice-periodic part of the phonon perturbation potential.⁵⁶ Since the dominant contribution to $g(\mathbf{k}, \mathbf{q})$ for the 2D mode comes from Na(2) atomic vibrations, we analyze the effect of

Na(2) motions on the Bi p_{xy} band, which is achieved by setting $\mathbf{e}_{\nu\mathbf{q}}^{(\kappa)}$ to 0 in eq 1 for Na(1) and Bi atoms. A similar analysis can be performed for Na(1) and Bi atomic motions, or using the Na s + Bi p_z band, but their contributions to $g(\mathbf{k}, \mathbf{q})$ are significantly smaller and do not affect our conclusions.

Electron-phonon scattering rates and charge transport

We interpolate the e -ph matrix elements on fine BZ grids with up to $130 \times 130 \times 90$ \mathbf{k} - and \mathbf{q} -points using maximally localized Wannier functions⁷⁰ generated with the Wannier90 code.⁷¹ We then compute the e -ph scattering rates at temperature T using⁵⁶

$$\Gamma_{n\mathbf{k}}(T) = \frac{2\pi}{\hbar} \sum_{m\nu\mathbf{q}} |g_{m\nu}(\mathbf{k}, \mathbf{q})|^2 \left[(N_{\nu\mathbf{q}} + 1 - f_{m\mathbf{k}+\mathbf{q}}) \delta(\varepsilon_{n\mathbf{k}} - \varepsilon_{m\mathbf{k}+\mathbf{q}} - \hbar\omega_{\nu\mathbf{q}}) + (N_{\nu\mathbf{q}} + f_{m\mathbf{k}+\mathbf{q}}) \delta(\varepsilon_{n\mathbf{k}} - \varepsilon_{m\mathbf{k}+\mathbf{q}} + \hbar\omega_{\nu\mathbf{q}}) \right], \quad (3)$$

where $\varepsilon_{n\mathbf{k}}$ and $f_{m\mathbf{k}+\mathbf{q}}$ are electron band energies and occupations, respectively, while $\hbar\omega_{\nu\mathbf{q}}$ and $N_{\nu\mathbf{q}}$ denote phonon energies and occupations. The electron and phonon occupations govern the temperature dependence of the e -ph scattering rates.

Using PERTURBO,⁵⁶ we obtain the carrier mobility as a function of temperature and doping concentration by solving the linearized Boltzmann transport equation:⁵⁶

$$\mathbf{F}_{n\mathbf{k}} = \mathbf{v}_{n\mathbf{k}} \tau_{n\mathbf{k}} + \frac{\tau_{n\mathbf{k}}}{\mathcal{N}_{\mathbf{q}}} \sum_{m,\nu\mathbf{q}} W_{n\mathbf{k},m\mathbf{k}+\mathbf{q}}^{\nu\mathbf{q}} \mathbf{F}_{m\mathbf{k}+\mathbf{q}} \quad (4)$$

where $W_{n\mathbf{k},m\mathbf{k}+\mathbf{q}}^{\nu\mathbf{q}}$ are phonon mode-dependent e -ph scattering rates from electronic state $|n\mathbf{k}\rangle$ to $|m\mathbf{k}+\mathbf{q}\rangle$ due to phonon mode (ν, \mathbf{q}) ; $\mathbf{v}_{n\mathbf{k}}$ are band velocities, $\tau_{n\mathbf{k}}$ are relaxation times, and $\mathcal{N}_{\mathbf{q}}$ is the number of \mathbf{q} -points used in the Brillouin zone summation. Above, $\mathbf{F}_{n\mathbf{k}}(T)$ is a term proportional to the first-order deviation of the electron occupations $f_{n\mathbf{k}}$ from their

equilibrium values $f_{n\mathbf{k}}^0$ due to the electric field \mathbf{E} , and is defined through

$$-f_{n\mathbf{k}}^0(1-f_{n\mathbf{k}}^0)\frac{e\mathbf{E}}{k_B T}\cdot\mathbf{F}_{n\mathbf{k}}=f_{n\mathbf{k}}-f_{n\mathbf{k}}^0. \quad (5)$$

The conductivity tensor $\sigma_{\alpha\beta}$ is computed using

$$\sigma_{\alpha\beta}=e^2\int dE(-\partial f^0/\partial E)\Sigma_{\alpha\beta}(E,T), \quad (6)$$

where α and β are Cartesian directions, and $\Sigma_{\alpha\beta}(E,T)$ is the transport distribution function at energy E and temperature T :³⁰

$$\Sigma_{\alpha\beta}(E,T)=\frac{1}{\mathcal{N}_{\mathbf{k}}\Omega}\sum_{n\mathbf{k}}v_{n\mathbf{k}}^\alpha\mathbf{F}_{n\mathbf{k}}^\beta(T)\delta(E-\varepsilon_{n\mathbf{k}}). \quad (7)$$

Here, $\mathcal{N}_{\mathbf{k}}$ is the number of \mathbf{k} -points in the Brillouin zone and Ω is the unit cell volume.

Acknowledgments

D.D. and J.P. thank Ivan Maliyov for fruitful discussions. This work was supported by the National Science Foundation under Grant No. DMR-1750613, which provided for method development, and Grant No. OAC-2209262, which provided for code development. M. B. was partially supported by the AFOSR and Clarkson Aerospace under Grant No. FA95502110460. This research used resources of the National Energy Research Scientific Computing Center (NERSC), a U.S. Department of Energy Office of Science User Facility located at Lawrence Berkeley National Laboratory, operated under Contract No. DE-AC02-05CH11231.

References

- [1] Armitage, N. P.; Mele, E. J.; Vishwanath, A. Weyl and Dirac semimetals in three-dimensional solids. *Rev. Mod. Phys.* **2018**, *90*, 015001.
- [2] He, L. P.; Hong, X. C.; Dong, J. K.; Pan, J.; Zhang, Z.; Zhang, J.; Li, S. Y. Quantum Transport Evidence for the Three-Dimensional Dirac Semimetal Phase in Cd_3As_2 . *Phys. Rev. Lett.* **2014**, *113*, 246402.
- [3] Liang, T.; Gibson, Q.; Ali, M. N.; Liu, M.; Cava, R. J.; Ong, N. P. Ultrahigh mobility and giant magnetoresistance in the Dirac semimetal Cd_3As_2 . *Nat. Mater.* **2015**, *14*, 280–284.
- [4] Cao, J. et al. Landau level splitting in Cd_3As_2 under high magnetic fields. *Nat. Commun.* **2015**, *6*, 7779.
- [5] Feng, J.; Pang, Y.; Wu, D.; Wang, Z.; Weng, H.; Li, J.; Dai, X.; Fang, Z.; Shi, Y.; Lu, L. Large linear magnetoresistance in Dirac semimetal Cd_3As_2 with Fermi surfaces close to the Dirac points. *Phys. Rev. B* **2015**, *92*, 081306.
- [6] Narayanan, A.; Watson, M. D.; Blake, S. F.; Bruyant, N.; Drigo, L.; Chen, Y. L.; Prabhakaran, D.; Yan, B.; Felser, C.; Kong, T.; Canfield, P. C.; Coldea, A. I. Linear Magnetoresistance Caused by Mobility Fluctuations in n -Doped Cd_3As_2 . *Phys. Rev. Lett.* **2015**, *114*, 117201.
- [7] Amarnath, R.; Bhargavi, K. S.; Kubakaddi, S. S. Phonon limited mobility in 3D Dirac semimetal Cd_3As_2 . *IOP Conf. Ser.: Mater. Sci. Eng.* **2019**, *561*, 012030.
- [8] Xiong, J.; Kushwaha, S. K.; Liang, T.; Krizan, J. W.; Hirschberger, M.; Wang, W.; Cava, R. J.; Ong, N. P. Evidence for the chiral anomaly in the Dirac semimetal Na_3Bi . *Science* **2015**, *350*, 413–416.

- [9] Xiong, J.; Kushwaha, S.; Krizan, J.; Liang, T.; Cava, R. J.; Ong, N. P. Anomalous Conductivity Tensor in the Dirac Semimetal Na_3Bi . *Europhys. Lett.* **2016**, *114*, 27002.
- [10] Li, C.-Z.; Wang, L.-X.; Liu, H.; Wang, J.; Liao, Z.-M.; Yu, D.-P. Giant negative magnetoresistance induced by the chiral anomaly in individual Cd_3As_2 nanowires. *Nat. Commun.* **2015**, *6*, 10137.
- [11] Wang, Z.; Sun, Y.; Chen, X.-Q.; Franchini, C.; Xu, G.; Weng, H.; Dai, X.; Fang, Z. Dirac semimetal and topological phase transitions in A_3Bi ($\text{A}=\text{Na}, \text{K}, \text{Rb}$). *Phys. Rev. B* **2012**, *85*, 195320.
- [12] Liang, A. et al. Electronic structure, Dirac points and Fermi arc surface states in three-dimensional Dirac semimetal Na_3Bi from angle-resolved photoemission spectroscopy. *Chin. Phys. B* **2016**, *25*, 077101.
- [13] Xu, S.-Y. et al. Observation of Fermi arc surface states in a topological metal. *Science* **2015**, *347*, 294–298.
- [14] Moll, P. J. W.; Nair, N. L.; Helm, T.; Potter, A. C.; Kimchi, I.; Vishwanath, A.; Analytis, J. G. Transport evidence for Fermi-arc-mediated chirality transfer in the Dirac semimetal Cd_3As_2 . *Nature* **2016**, *535*, 266–270.
- [15] Collins, J. L.; Tadich, A.; Wu, W.; Gomes, L. C.; Rodrigues, J. N. B.; Liu, C.; Hellstedt, J.; Ryu, H.; Tang, S.; Mo, S.-K.; Adam, S.; Yang, S. A.; Fuhrer, M. S.; Edmonds, M. T. Electric-field-tuned topological phase transition in ultrathin Na_3Bi . *Nature* **2018**, *564*, 390–394.
- [16] Xia, H.; Li, Y.; Cai, M.; Qin, L.; Zou, N.; Peng, L.; Duan, W.; Xu, Y.; Zhang, W.; Fu, Y.-S. Dimensional Crossover and Topological Phase Transition in Dirac Semimetal Na_3Bi Films. *ACS Nano* **2019**, *13*, 9647–9654.
- [17] Geim, A. K.; Novoselov, K. S. The rise of graphene. *Nat. Mater.* **2007**, *6*, 183.

- [18] Hills, R. D. Y.; Kusmartseva, A.; Kusmartsev, F. V. Current-voltage characteristics of Weyl semimetal semiconducting devices, Veselago lenses, and hyperbolic Dirac phase. *Phys. Rev. B* **2017**, *95*, 214103.
- [19] Yanez, W. et al. Spin and Charge Interconversion in Dirac-Semimetal Thin Films. *Phys. Rev. Appl.* **2021**, *16*, 054031.
- [20] Sie, E. J. et al. An ultrafast symmetry switch in a Weyl semimetal. *Nature* **2019**, *565*, 61–66.
- [21] Zhang, M. Y.; Wang, Z. X.; Li, Y. N.; Shi, L. Y.; Wu, D.; Lin, T.; Zhang, S. J.; Liu, Y. Q.; Liu, Q. M.; Wang, J.; Dong, T.; Wang, N. L. Light-Induced Subpicosecond Lattice Symmetry Switch in MoTe₂. *Phys. Rev. X* **2019**, *9*, 021036.
- [22] Vaswani, C. et al. Light-Driven Raman Coherence as a Nonthermal Route to Ultrafast Topology Switching in a Dirac Semimetal. *Phys. Rev. X* **2020**, *10*, 021013.
- [23] Xiao, J.; Wang, Y.; Wang, H.; Pemmaraju, C. D.; Wang, S.; Muscher, P.; Sie, E. J.; Nyby, C. M.; Devereaux, T. P.; Qian, X.; Zhang, X.; Lindenberg, A. M. Berry curvature memory through electrically driven stacking transitions. *Nat. Phys.* **2020**, *16*, 1028.
- [24] Disa, A. S.; Nova, T. F.; Cavalleri, A. Engineering crystal structures with light. *Nat. Phys.* **2021**, *17*, 1087–1092.
- [25] Sklyadneva, I.; Heid, R.; Echenique, P. M.; Chulkov, E. V. Electron-phonon coupling in the magnetic Weyl semimetal ZrCo₂Sn. *Phys. Rev. B* **2021**, *103*, 024303.
- [26] Liu, P.-F.; Li, J.; Zhang, C.; Tu, X.-H.; Zhang, J.; Zhang, P.; Wang, B.-T.; Singh, D. J. Type-II Dirac cones and electron-phonon interaction in monolayer biphenylene from first-principles calculations. *Phys. Rev. B* **2021**, *104*, 235422.
- [27] Bernardi, M. First-principles dynamics of electrons and phonons. *Eur. Phys. J. B* **2016**, *89*, 239.

- [28] Agapito, L. A.; Bernardi, M. Ab initio electron-phonon interactions using atomic orbital wave functions. *Phys. Rev. B* **2018**, *97*, 235146.
- [29] Bernardi, M.; Vigil-Fowler, D.; Lischner, J.; Neaton, J. B.; Louie, S. G. Ab Initio Study of Hot Carriers in the First Picosecond after Sunlight Absorption in Silicon. *Phys. Rev. Lett.* **2014**, *112*, 257402.
- [30] Zhou, J.-J.; Bernardi, M. Ab initio electron mobility and polar phonon scattering in GaAs. *Phys. Rev. B* **2016**, *94*, 201201(R).
- [31] Zhou, J.-J.; Hellman, O.; Bernardi, M. Electron-Phonon Scattering in the Presence of Soft Modes and Electron Mobility in SrTiO₃ Perovskite from First Principles. *Phys. Rev. Lett.* **2018**, *121*, 226603.
- [32] Zhou, J.-J.; Bernardi, M. Predicting charge transport in the presence of polarons: The beyond-quasiparticle regime in SrTiO₃. *Phys. Rev. Res.* **2019**, *1*, 033138.
- [33] Park, C.-H.; Giustino, F.; Cohen, M. L.; Louie, S. G. Velocity Renormalization and Carrier Lifetime in Graphene from the Electron-Phonon Interaction. *Phys. Rev. Lett.* **2007**, *99*, 086804.
- [34] Floris, A.; Sanna, A.; Massidda, S.; Gross, E. K. U. Two-band superconductivity in Pb from ab initio calculations. *Phys. Rev. B* **2007**, *75*, 054508.
- [35] Li, W. Electrical transport limited by electron-phonon coupling from Boltzmann transport equation: An ab initio study of Si, Al, and MoS₂. *Phys. Rev. B* **2015**, *92*, 075405.
- [36] Liu, T.-H.; Zhou, J.; Liao, B.; Singh, D. J.; Chen, G. First-principles mode-by-mode analysis for electron-phonon scattering channels and mean free path spectra in GaAs. *Phys. Rev. B* **2017**, *95*, 075206.
- [37] Ma, J.; Nissimagoudar, A. S.; Li, W. First-principles study of electron and hole mobilities of Si and GaAs. *Phys. Rev. B* **2018**, *97*, 045201.

- [38] Ponc e, S.; Margine, E. R.; Giustino, F. Towards predictive many-body calculations of phonon-limited carrier mobilities in semiconductors. *Phys. Rev. B* **2018**, *97*, 121201.
- [39] Liu, Z. K.; Zhou, B.; Zhang, Y.; Wang, Z. J.; Weng, H. M.; Prabhakaran, D.; Mo, S.-K.; Shen, Z. X.; Fang, Z.; Dai, X.; Hussain, Z.; Chen, Y. L. Discovery of a Three-Dimensional Topological Dirac Semimetal, Na₃Bi. *Science* **2014**, *343*, 864–867.
- [40] Kushwaha, S. K.; Krizan, J. W.; Feldman, B. E.; Gyenis, A.; Randeria, M. T.; Xiong, J.; Xu, S.-Y.; Alidoust, N.; Belopolski, I.; Liang, T.; Zahid Hasan, M.; Ong, N. P.; Yazdani, A.; Cava, R. J. Bulk Crystal Growth and Electronic Characterization of the 3D Dirac Semimetal Na₃Bi. *APL Mater.* **2015**, *3*, 041504.
- [41] Edmonds, M. T.; Collins, J. L.; Hellerstedt, J.; Yudhistira, I.; Gomes, L. C.; Rodrigues, J. N. B.; Adam, S.; Fuhrer, M. S. Spatial charge inhomogeneity and defect states in topological Dirac semimetal thin films of Na₃Bi. *Sci. Adv.* **2017**, *3*, eaao6661.
- [42] Di Bernardo, I.; Collins, J.; Wu, W.; Zhou, J.; Yang, S. A.; Ju, S.; Edmonds, M. T.; Fuhrer, M. S. Importance of Interactions for the Band Structure of the Topological Dirac Semimetal Na₃Bi. *Phys. Rev. B* **2020**, *102*, 045124.
- [43] Yuan, H. F.; Xu, W.; Zhao, X. N.; Song, D.; Zhang, G. R.; Xiao, Y. M.; Ding, L.; Peeters, F. M. Quantum and transport mobilities of a Na₃Bi-based three-dimensional Dirac system. *Phys. Rev. B* **2019**, *99*, 235303.
- [44] H ubener, H.; Sentef, M. A.; De Giovannini, U.; Kemper, A. F.; Rubio, A. Creating stable Floquet–Weyl semimetals by laser-driving of 3D Dirac materials. *Nat. Commun.* **2017**, *8*, 13940.
- [45] Tancogne-Dejean, N.; Eich, F. G.; Rubio, A. Effect of spin-orbit coupling on the high harmonics from the topological Dirac semimetal Na₃Bi. *npj Comput. Mater.* **2022**, *8*, 145.

- [46] Martin, R. M. *Electronic Structure: Basic Theory and Practical Methods*; Cambridge University Press, 2004.
- [47] Baroni, S.; de Gironcoli, S.; Dal Corso, A.; Giannozzi, P. Phonons and related crystal properties from density-functional perturbation theory. *Rev. Mod. Phys.* **2001**, *73*, 515–562.
- [48] Hybertsen, M. S.; Louie, S. G. Electron correlation in semiconductors and insulators: Band gaps and quasiparticle energies. *Phys. Rev. B* **1986**, *34*, 5390–5413.
- [49] Schweicher, G. et al. Chasing the “Killer” Phonon Mode for the Rational Design of Low-Disorder, High-Mobility Molecular Semiconductors. *Adv. Mater.* **2019**, *31*, 1902407.
- [50] Jenkins, G. S.; Lane, C.; Barbiellini, B.; Sushkov, A. B.; Carey, R. L.; Liu, F.; Krizan, J. W.; Kushwaha, S. K.; Gibson, Q.; Chang, T.-R.; Jeng, H.-T.; Lin, H.; Cava, R. J.; Bansil, A.; Drew, H. D. Three-dimensional Dirac cone carrier dynamics in Na_3Bi and Cd_3As_2 . *Phys. Rev. B* **2016**, *94*, 085121.
- [51] Shao, D.; Ruan, J.; Wu, J.; Chen, T.; Guo, Z.; Zhang, H.; Sun, J.; Sheng, L.; Xing, D. Strain-induced quantum topological phase transitions in Na_3Bi . *Phys. Rev. B* **2017**, *96*, 075112.
- [52] Chiu, W.-C.; Singh, B.; Mardanya, S.; Nokelainen, J.; Agarwal, A.; Lin, H.; Lane, C.; Pussi, K.; Barbiellini, B.; Bansil, A. Topological Dirac Semimetal Phase in Bismuth Based Anode Materials for Sodium-Ion Batteries. *Condens. Matter* **2020**, *5*, 39.
- [53] Mounet, N. Structural, vibrational and thermodynamic properties of carbon allotropes from first-principles: diamond, graphite, and nanotubes. *Masters thesis* **2005**,
- [54] Giannozzi, P. et al. QUANTUM ESPRESSO: a modular and open-source software project for quantum simulations of materials. *J. Phys. Condens. Matter* **2009**, *21*, 395502.

- [55] Cheng, X.; Li, R.; Sun, Y.; Chen, X.-Q.; Li, D.; Li, Y. Ground-State Phase in the Three-Dimensional Topological Dirac Semimetal Na₃Bi. *Phys. Rev. B* **2014**, *89*, 245201.
- [56] Zhou, J.-J.; Park, J.; Lu, I.-T.; Maliyov, I.; Tong, X.; Bernardi, M. Perturbo: A software package for ab initio electron–phonon interactions, charge transport and ultrafast dynamics. *Comput. Phys. Commun.* **2021**, *264*, 107970.
- [57] Pizzi, G.; Milana, S.; Ferrari, A. C.; Marzari, N.; Gibertini, M. Shear and Breathing Modes of Layered Materials. *ACS Nano* **2021**, *15*, 12509–12534.
- [58] Neupane, M.; Xu, S.-Y.; Sankar, R.; Alidoust, N.; Bian, G.; Liu, C.; Belopolski, I.; Chang, T.-R.; Jeng, H.-T.; Lin, H.; Bansil, A.; Chou, F.; Hasan, M. Z. Observation of a three-dimensional topological Dirac semimetal phase in high-mobility Cd₃As₂. *Nature Communications* **2014**, *5*, 3786.
- [59] Park, C.-H.; Bonini, N.; Sohler, T.; Samsonidze, G.; Kozinsky, B.; Calandra, M.; Mauri, F.; Marzari, N. Electron–Phonon Interactions and the Intrinsic Electrical Resistivity of Graphene. *Nano Lett.* **2014**, *14*, 1113–1119.
- [60] Tong, X.; Bernardi, M. Toward precise simulations of the coupled ultrafast dynamics of electrons and atomic vibrations in materials. *Phys. Rev. Res.* **2021**, *3*, 023072.
- [61] Desai, D. C.; Zviazhynski, B.; Zhou, J.-J.; Bernardi, M. Magnetotransport in semiconductors and two-dimensional materials from first principles. *Phys. Rev. B* **2021**, *103*, L161103.
- [62] Dong, X.-X.; Chen, J.-X.; Wang, Y.; Lv, Z.-L.; Wang, H.-Y. Electronic, elastic and lattice dynamic properties of the topological Dirac semimetal Na₃Bi. *Mater. Res. Express* **2019**, *6*, 076308.
- [63] Merlin, R. Generating coherent THz phonons with light pulses. *Solid State Commun.* **1997**, *102*, 207.

- [64] Bohnen, K.-P.; Heid, R.; Renker, B. Phonon Dispersion and Electron-Phonon Coupling in MgB_2 and AlB_2 . *Phys. Rev. Lett.* **2001**, *86*, 5771–5774.
- [65] An, J. M.; Pickett, W. E. Superconductivity of MgB_2 : Covalent Bonds Driven Metallic. *Phys. Rev. Lett.* **2001**, *86*, 4366–4369.
- [66] Perdew, J. P.; Ruzsinszky, A.; Csonka, G. I.; Vydrov, O. A.; Scuseria, G. E.; Constantin, L. A.; Zhou, X.; Burke, K. Restoring the Density-Gradient Expansion for Exchange in Solids and Surfaces. *Phys. Rev. Lett.* **2008**, *100*, 136406.
- [67] van Setten, M.; Giantomassi, M.; Bousquet, E.; Verstraete, M.; Hamann, D.; Gonze, X.; Rignanese, G.-M. The PseudoDojo: Training and grading a 85 element optimized norm-conserving pseudopotential table. *Comput. Phys. Commun.* **2018**, *226*, 39–54.
- [68] Sangalli, D. et al. Many-Body Perturbation Theory Calculations Using the Yambo Code. *J. Phys. Condens. Matter* **2019**, *31*, 325902.
- [69] Bruneval, F.; Gonze, X. Accurate GW self-energies in a plane-wave basis using only a few empty states: Towards large systems. *Phys. Rev. B* **2008**, *78*, 085125.
- [70] Marzari, N.; Mostofi, A. A.; Yates, J. R.; Souza, I.; Vanderbilt, D. Maximally localized Wannier functions: Theory and applications. *Rev. Mod. Phys.* **2012**, *84*, 1419–1475.
- [71] Mostofi, A. A.; Yates, J. R.; Pizzi, G.; Lee, Y.-S.; Souza, I.; Vanderbilt, D.; Marzari, N. An updated version of WANNIER90: A tool for obtaining maximally-localised Wannier functions. *Comput. Phys. Commun.* **2014**, *185*, 2309 – 2310.